(Fig. 4) supports the hypothesis that the integumentary structures in Ornithischia, already described in *Psittacosaurus* (*12*) and *Tianyulong* (*13*), could be homologous to the "protofeathers" in non-avian theropods. In any case, it indicates that those protofeather-like structures were probably widespread in Dinosauria, possibly even in the earliest members of the clade. Further, the ability to form simple monofilaments and more complex compound structures is potentially nested within the archosauromorph clade, as exemplified by *Longisquama* (*23*), pterosaurs (*24*), ornithischians, and theropods (including birds).

In *Kulindadromeus* and most ornithuromorph birds (*17*, *25*), the distal hindlimb is extensively covered by scales and devoid of featherlike structures. This condition might thus be primitive in dinosaurs. Both paleontological and genetic evidence, however, suggests that the pedal scales of ornithuromorph birds are secondarily derived from feathers. In avialan evolution, leg feathers were reduced gradually in a distal-to-proximal direction, with eventual loss of the distal feathers and appearance of pedal scales in ornithuromorphs (*25*). Further, evo-devo experiments (*26*, *27*) show that feathers in extant birds are the default fate of the avian epidermis, and that the formation of avian scales requires the inhibition of feather development. The local formation of scales requires the inhibition of epidermal outgrowth, regulated by the *sonic hedgehog* pathway; this inhibition is partially lost in the case of breeds with feathered feet (*27*). Therefore, it is possible that the extensively scaled distal hindlimbs in *Kulindadromeus* might be explained by similar local and partial inhibition in the development of featherlike structures. The preservation of featherlike structures and scales in the basal neornithischian *Kulindadromeus*, and their similarity to structures that are present in diverse theropods and ornithuromorph birds, thus strongly suggest that deep homology mechanisms (*28*) explain the complex distribution of skin appendages within dinosaurs (*23*).

REFERENCES AND NOTES

1. M. A. Norell, X. Xu, *Annu. Rev. Earth Planet. Sci.* **33**, 277–299 (2005).
2. T. Lingham-Soliar, A. Feduccia, X. Wang, *Proc. Biol. Sci.* **274**, 2823 (2007).
3. F. Zhang, Z. Zhou, G. Dyke, *Geol. J.* **41**, 395 (2006).
4. T. Lingham-Soliar, *Proc. Biol. Sci.* **275**, 775–780 (2008).
5. D. Hu, L. Hou, L. Zhang, X. Xu, *Nature* **461**, 640–643 (2009).
6. S. L. Brusatte *et al.*, *Earth Sci. Rev.* **101**, 68–100 (2010).
7. X. Xu, H. You, K. Du, F. Han, *Nature* **475**, 465–470 (2011).
8. P. Godefroit *et al.*, *Nat. Commun.* **4**, 1394 (2013).
9. P. Godefroit *et al.*, *Nature* **498**, 359–362 (2013).
10. F. Zhang *et al.*, *Nature* **463**, 1075–1078 (2010).
11. Q. Li *et al.*, *Science* **327**, 1369–1372 (2010).
12. G. Mayr, D. S. Peters, G. Plodowski, O. Vogel, *Naturwissenschaften* **89**, 361–365 (2002).
13. X.-T. Zheng, H.-L. You, X. Xu, Z.-M. Dong, *Nature* **458**, 333–336 (2009).
14. O. W. M. Rauhut, C. Foth, H. Tischlinger, M. A. Norell, *Proc. Natl. Acad. Sci. U.S.A.* **109**, 11746–11751 (2012).
15. See the supplementary materials on *Science* Online.
16. R. J. Butler, P. Upchurch, D. B. Norman, *J. Syst. Palaeontology* **6**, 1–40 (2008).
17. A. M. Lucas, P. R. Stettenheim, *Avian Anatomy, Integument* (U.S. Department of Agriculture, Washington, DC, 1972).
18. M. K. Vickarious, T. Maryanska, D. B. Weishampel, in *The Dinosauria 2nd edn*, D. B. Weishampel, P. Dodson, H. Osmolska, Eds. (Univ. of California Press, Berkeley, CA, 2004), pp. 363–392.
19. P. R. Bell, *PLOS ONE* **7**, e31295 (2012).
20. P. J. Currie, P. J. Chen, *Can. J. Earth Sci.* **38**, 1705–1727 (2001).
21. X. Xu, X. Zheng, H. You, *Nature* **464**, 1338–1341 (2010).
22. F. Zhang, Z. Zhou, X. Xu, X. Wang, C. Sullivan, *Nature* **455**, 1105–1108 (2008).
23. M. Buchwitz, S.Voigt, *Paläontol. Z.* **86**, 313 (2012).
24. X. Wang, Z. Zhou, F. Zhang, X. Xu, *Chin. Sci. Bull.* **47**, 226 (2002).
25. X. Zheng *et al.*, *Science* **339**, 1309–1312 (2013).
26. D. Dhouailly, *J. Anat.* **214**, 587–606 (2009).
27. F. Prin, D. Dhouailly, *Int. J. Dev. Biol.* **48**, 137–148 (2004).
28. N. Shubin, C. Tabin, S. Carroll, *Nature* **388**, 639–648 (1997).

RNA FUNCTION

Ribosome stalling induced by mutation of a CNS-specific tRNA causes neurodegeneration

Ryuta Ishimura,[1]* Gabor Nagy,[1]* Ivan Dotu,[2] Huihao Zhou,[3] Xiang-Lei Yang,[3] Paul Schimmel,[3] Satoru Senju,[4] Yasuharu Nishimura,[4] Jeffrey H. Chuang,[2] Susan L. Ackerman[1]†

In higher eukaryotes, transfer RNAs (tRNAs) with the same anticodon are encoded by multiple nuclear genes, and little is known about how mutations in these genes affect translation and cellular homeostasis. Similarly, the surveillance systems that respond to such defects in higher eukaryotes are not clear. Here, we discover that loss of GTPBP2, a novel binding partner of the ribosome recycling protein Pelota, in mice with a mutation in a tRNA gene that is specifically expressed in the central nervous system causes ribosome stalling and widespread neurodegeneration. Our results not only define GTPBP2 as a ribosome rescue factor but also unmask the disease potential of mutations in nuclear-encoded tRNA genes.

In higher eukaryotes, the nuclear genome typically contains several hundred transfer RNA (tRNA) genes, which fall into isoacceptor groups, each representing an anticodon (*1*). Relative to the total number of tRNA genes, the number of isodecoders—i.e., tRNA molecules with the same anticodon but differences in the tRNA body—increases dramatically with organismal complexity, which leads to speculation that isodecoders might not be fully redundant with one another (*2*). Overexpression of reporter constructs with rare codons that are decoded by correspondingly low-abundance tRNAs in bacteria and yeast, or mutations in single-copy

mitochondrial tRNA genes, may result in stalled elongation complexes (*3–5*). However, the consequences of mutations in multicopy, nuclear-encoded tRNA isodecoder genes or in the surveillance systems that eliminate the effect of such tRNA mutations are not known in higher eukaryotes.

The *nmf205* mutation was identified in an *N*-ethyl-*N*-nitorosurea mutagenesis screen of C57BL/6J (B6J) mice for neurological phenotypes (*6*). B6J-*nmf205*^{−/−} mice were indistinguishable from wild-type mice at 3 weeks of age but showed clear truncal ataxia at 6 weeks (movie S1). Mice died at 8 to 9 weeks with severe locomotor deficits. Progressive apoptosis of neurons in the inner granule layer (IGL) in the mutant cerebellum was initially observed between 3 and 4 weeks of age (Fig. 1, A to H). Apoptosis of mutant granule cells in the dentate gyrus, CA2 pyramidal neurons, and layer IV cortical neurons occurred between 5 and 8 weeks of age (Fig. 1, I and J, and fig. S1, A to H). Further, many neurons in the retina—including photoreceptors and amacrine, horizontal, and ganglion cells—degenerated during this time (Fig. 1, K and L, and fig. S1, I to T).

[1]Howard Hughes Medical Institute and The Jackson Laboratory, 600 Main Street, Bar Harbor, ME 04609, USA. [2]The Jackson Laboratory for Genomic Medicine, 263 Farmington Avenue, Farmington, CT 06030, USA. [3]The Skaggs Institute for Chemical Biology, The Scripps Research Institute, 10550 North Torrey Pines Road, La Jolla, CA 92037, USA. [4]Department of Immunogenetics, Graduate School of Medical Sciences, Kumamoto University, Honjo 1-1-1, Chuo-ku, Kumamoto 860-8556, Japan.
*These authors contributed equally to this work. †Corresponding author. E-mail: susan.ackerman@jax.org

Histological analysis of other organs did not reveal obvious pathology nor was neurodegeneration observed in mice heterozygous for this mutation.

We identified the *nmf205* mutation as a point mutation in the consensus splice donor site of intron 6 of *Gtpbp2* that results in misspliced mRNAs with premature stop codons (fig. S2). Accordingly, Western blot analysis of mutant cerebellar extracts failed to detect GTPBP2 (Fig. 2A). Complementation tests using *nmf205* mice and mice with a targeted deletion of *Gtpbp2* confirmed that loss of *Gtpbp2* results in neurodegeneration (fig. S3).

GTPBP2 shares domain homology with a translational guanosine triphosphatase family that is characterized by the no-go and nonstop decay pathways ribosome-recycling protein Hbs1 and the eukaryotic release factor eRF3, which bind Dom34 and eRF1, respectively (fig. S4A) (*7–9*). Although no interaction was observed between GTPBP2 and eRF1 in coimmunoprecipitation assays, Pelota (the mammalian Dom34 homolog) was immunoprecipitated by GTPBP2 (Fig. 2B). The glutathione *S*-transferase–GTPBP2 fusion protein (GST-GTPBP2) also pulled down Pelota from brain extracts, which demonstrated that GTPBP2 can interact with endogenous Pelota (Fig. 2C). Affinity capture of bacterially expressed GTPBP2 by Pelota demonstrated that these proteins directly interact (Fig. 2D).

Analysis of mice from our mapping cross and B6J.BALB^{Chr1} congenic mice revealed that homo- or heterozygosity for a BALB/cJ-derived locus (*Mod205*) on distal chromosome 1 suppressed neurodegeneration in *nmf205*$^{-/-}$ and *Gtpbp2*$^{-/-}$

mice (fig. S5). Mutant mice carrying this BALB locus routinely survived to 18 months or longer. Further analysis of multiple other inbred strains including C57BL/6NJ (B6N) suggested that neurodegeneration in B6J-*nmf205*$^{-/-}$ mice is likely due to an epistatic mutation in the B6J strain (table S1).

One single-nucleotide polymorphism (SNP) in the *Mod205* region, *rs46447118*, was determined to be a T in the B6J genome but a C in all other tested strains (fig. S6A). This SNP resides at nucleotide 50 in the stem of the T loop of *n-Tr20*, one of five isodecoders of the nuclear-encoded tRNA$^{Arg}_{UCU}$ family (fig. S6, B and C). Orthologs of *n-Tr20* are widely found in both vertebrates and invertebrates (fig. S6D). We assayed *n-Tr20* aminoacylation and found that the majority of this tRNA was charged in the B6N brain, but very low levels were observed in B6J (Fig. 3A). Mutations in the T stem of tRNAs have been shown to affect pre-tRNA processing and function (*10, 11*). In agreement, a 105-nucleotide (nt) band was detected in the B6J brain, which was confirmed to be the pre-tRNA retaining the leader and trailer sequences (Fig. 3B and fig. S7A). In wild-type brains, the pre-tRNA is 115 nt, which suggests the C-to-T mutation changes the length of the primary transcript. Examination of *n-Tr20* processing in reciprocal congenic strains confirmed that this mutation underlies the observed maturation defect (fig. S7B).

To confirm that loss of mature *n-Tr20* underlies neurodegeneration in B6J-*nmf205*$^{-/-}$ mice (which are mutant for both *Gtpbp2* and *n-Tr20*), B6J mice transgenically expressing wild-type *n-Tr20* and harboring the *nmf205* mutation (Tg; *nmf205*$^{-/-}$) were examined (fig. S8, A and B).

At 6 months of age, neuron death was greatly attenuated in the brain and retina (Fig. 3C).

Although *Gtpbp2* is widely expressed (fig. S4B) (*12, 13*), pathology in mice lacking this gene is restricted to the CNS. In contrast to other members of the tRNA$^{Arg}_{UCU}$ family, expression of *n-Tr20* and its human ortholog were surprisingly confined to the CNS (Fig. 3D and fig. S8, C and D). In addition, overall expression of the tRNA$^{Arg}_{UCU}$ isodecoder family was higher in the CNS than in other tissues (Fig. 3D). Compared with levels of processed *n-Tr20* in age-matched B6N brains, which show steady postnatal expression, levels in the B6J brain fell from 50% of B6N levels at postnatal day 0 (P0) to 19% by P30 (Fig. 3E), and a concomitant increase in immature *n-Tr20* was also observed. Although B6J brains have a slight increase in expression of the other members of the tRNA$^{Arg}_{UCU}$ family, a dramatic reduction in the B6J total tRNA$^{Arg}_{UCU}$ pool was observed, which demonstrated that *n-Tr20* normally makes up ~60% of the expression of this isodecoder family (Fig. 3F and fig. S9). Spatial differences in processing of mutant *n-Tr20* were also observed within the B6J brain with significantly lower levels of processed and higher levels of unprocessed *n-Tr20* in the cerebellum compared with the cortex and hippocampus (Fig. 3G). Together, these data define a CNS-specific tRNA in which levels of mature transcript correlate with the onset and severity of cell death in *Gtpbp2*-deficient mice.

We hypothesized that the *n-Tr20* mutation causes ribosome stalling at AGA codons that is exacerbated in the absence of *Gtpbp2*. To test this, we generated ribosome-profiling libraries
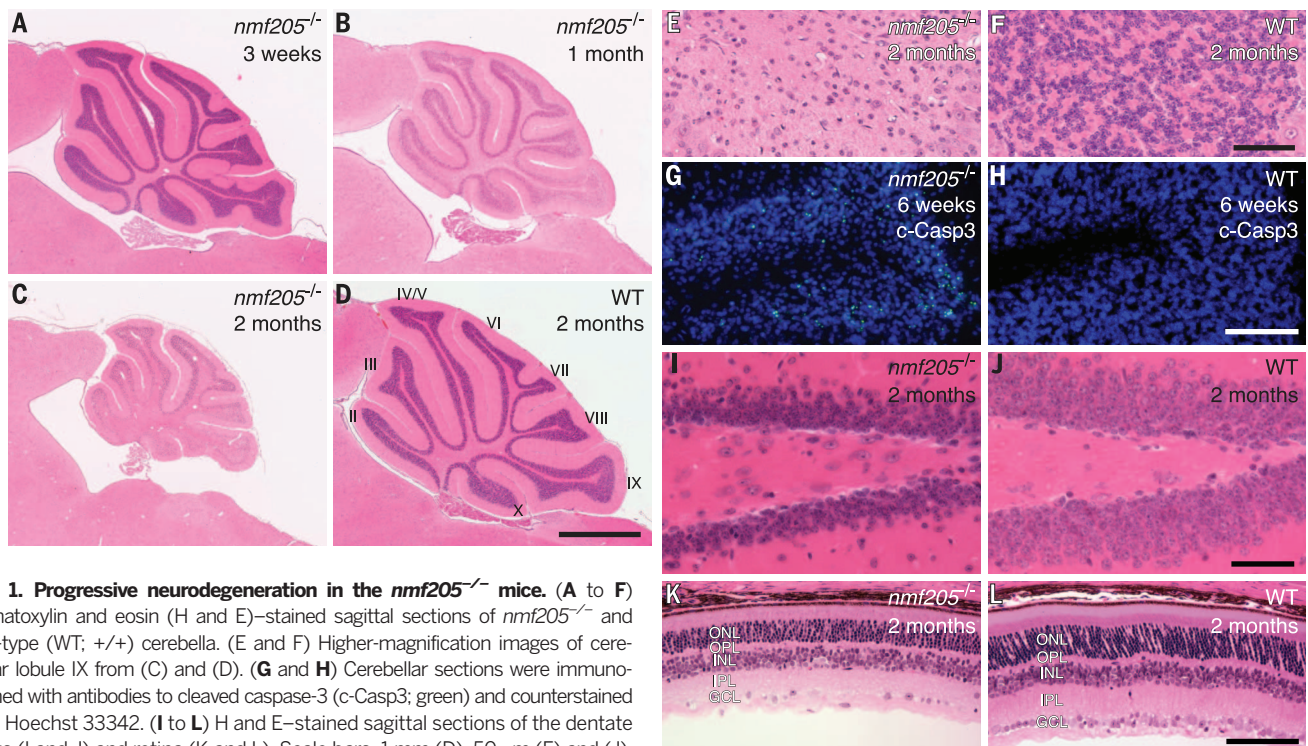

Fig. 1. Progressive neurodegeneration in the *nmf205*$^{-/-}$ mice. (**A** to **F**) Hematoxylin and eosin (H and E)–stained sagittal sections of *nmf205*$^{-/-}$ and wild-type (WT; +/+) cerebella. (E and F) Higher-magnification images of cerebellar lobule IX from (C) and (D). (**G** and **H**) Cerebellar sections were immunostained with antibodies to cleaved caspase-3 (c-Casp3; green) and counterstained with Hoechst 33342. (**I** to **L**) H and E–stained sagittal sections of the dentate gyrus (I and J) and retina (K and L). Scale bars, 1 mm (D), 50 μm (F) and (J), and 100 μm (H) and (L). ONL, outer nuclear layer; OPL, outer plexiform layer; INL, inner nuclear layer; IPL, inner plexiform layer; GCL, ganglion cell layer.

from cerebella of 3-week-old B6J (*n-Tr20* mutant), B6J.B6N[n–Tr20] (*n-Tr20* wild-type), B6J-*nmf205*^{−/−} (*Gtpbp2*^{−/−}; *n-Tr20* mutant), and B6J.B6N[n–Tr20]; *nmf205*^{−/−} (*Gtpbp2*^{−/−}; *n-Tr20* wild-type) mice (14–16). We calculated the pause strength for each codon in the ribosome A site for every gene (figs. S10 to S14). Consistent with prior studies, we observed thousands of strong pauses (P of ≥10 standard deviations above background), including a

Fig. 2. The *nmf205* mutation disrupts the Pelota-interacting protein, GTPBP2. (**A**) Western blot analysis of GTPBP2 in wild-type (WT, +/+) and *nmf205*^{−/−} (−/−) cerebellar extracts using antibodies to the N-terminal of GTPBP2. Glyceraldehyde-3-phosphate dehydrogenase (GAPDH) was used as a loading control. (**B**) Coimmuno-precipitation (IP) from human embryonic kidney–293T cells cotransfected with FLAG-fusion proteins as indicated, and Pelota fused to hemagglutinin (Pelota-HA). Input levels were determined by immunoblotting (IB). (**C**) GST pull-down (PD) assay of brain lysate (BL). The pull-down eluate and GST-fused baits were immunoblotted as indicated. (**D**) Bacterially expressed myelin basic protein (MBP) fused with GTPBP2 and labeled with histidine (MGP-GTPBP2-His) or MBP-His were purified and were incubated with GST or GST-Pelota. GST pull-down products (top) and input (middle and bottom) were immunoblotted with anti-His antibody (two and middle) or visualized by Coomassie blue (bottom).
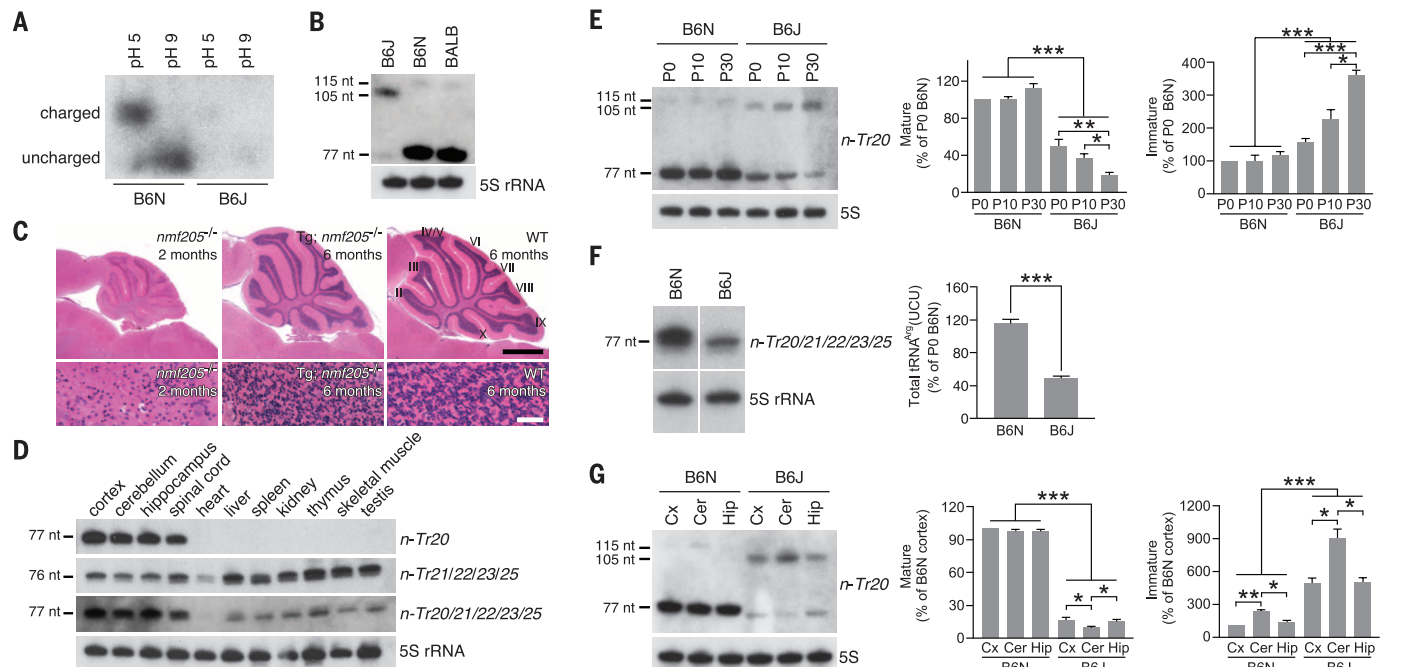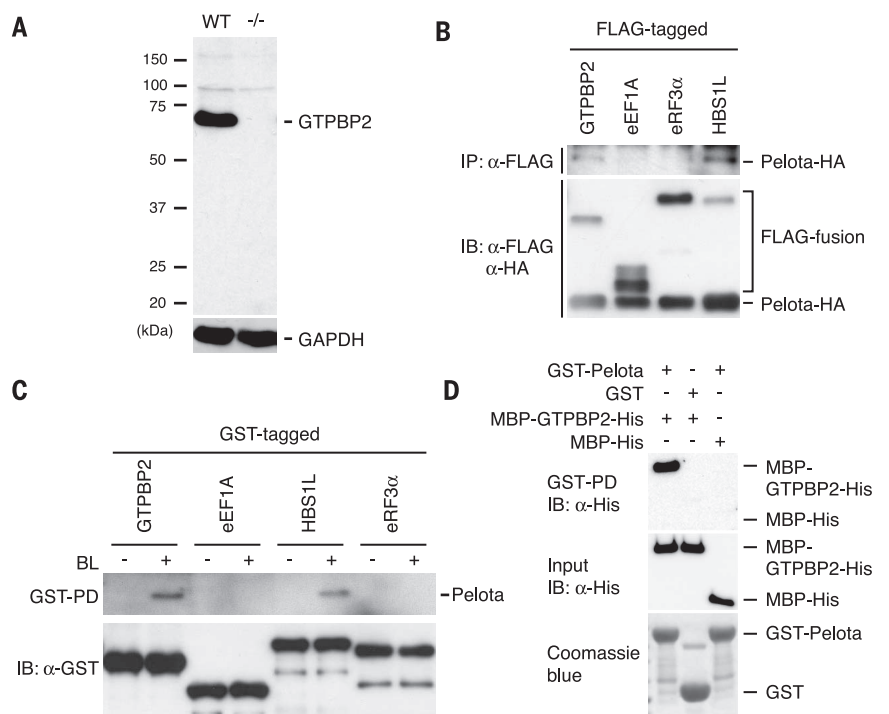
Fig. 3. Mutation of the CNS-specific tRNA^Arg gene *n-Tr20* underlies *nmf205*-mediated neurodegeneration. (**A**) Acylated (pH 5) and deacy-lated (pH 9) *n-Tr20* detected by Northern blot analysis of acid gels from polyacrylamide gel electrophoresis. (**B**) Northern blot analysis of *n-Tr20* in brain RNA from P30 mice. (**C**) H and E–stained sagittal sections of cerebella from 2-month-old B6J-*nmf205*^{−/−} (*nmf205*^{−/−}), 6-month-old Tg(n-Tr20^B6N) 609; B6J-*nmf205*^{−/−}, and 6-month-old wild-type (WT; B6J) mice. Higher magnification images of lobule IX from top panels are shown at the bottom . Scale bars in (C): 1 mm (top) and 50 μm (bottom). (**D**) Northern blot analysis of *n-Tr20*, its isodecoders, and all tRNA^Arg_UCU genes. Ribosomal RNA (5S rRNA) was used as loading control. (**E**) Northern blot analysis of *n-Tr20* in P0, P10, and P30 B6N and B6J brain RNA. Mature and immature *n-Tr20* transcripts were quantified relative to the P0 B6N brain. (**F**) Northern blot analysis of *n-Tr20* in the P30 B6N and B6J cortex (Cx), cerebellum (Cer), and hippocampus (Hip). Mature and immature *n-Tr20* was quantified relative to the B6N cortex. (**G**) Northern blot analysis of B6N and B6J P30 brain RNA using pooled probes to *n-Tr20/21/22/23/25* tRNAs. Bands were quantified relative to the P0 B6N brain. Error bars indicate SEMs. All data are represent-ative of independent experiments with three or more mice. *P < 0.05, **P < 0.005 and ***P < 0.0005 (two-tailed Student's *t* test).

well-studied pause in *Xbp1*, in each genotype (Fig. 4, A and B; fig. S15A; tables S2, A to H; and table S3) (*16*, *17*). However, no significant differences in pause number occurred between genotypes.

We then determined the number of pauses at AGA codons (Fig. 4C and fig. S15B). In the B6J.B6N^{n-Tr20} and B6J.B6N^{n-Tr20}; *nmf205*$^{-/-}$ cerebellum, few strong AGA pauses were observed (Fig. 4D and tables S2, I to P). Demonstrating the effect of impaired *n-Tr20* processing, a threefold increase in strong AGA pauses was observed in the B6J

cerebellum. However, the number of AGA pauses increased dramatically in the B6J-*nmf205*$^{-/-}$ cerebellum (Fig. 4, D and E, and fig. S16). Although only a limited number of AGA codons exhibited strong pausing (P ≥ 10), strong pause sites and scores overall showed significant concordance in biological replicates (*18*) (fig. S14 and table S4). Gene ontology analysis of transcripts with strong pauses in the B6J-*nmf205*$^{-/-}$ cerebellum showed enrichment for translation-related genes, among others (table S2Q).

Reads at AGA codons in B6J and B6J-*nmf205*$^{-/-}$ cerebella were 1.6 and 2.8 times background expectations, respectively, whereas unusual AGA pausing was not observed in cerebellar libraries from B6J.B6N^{n-Tr20} and B6J.B6N^{n-Tr20}; *nmf205*$^{-/-}$ mice (Fig. 4F). To determine whether the increase in ribosome pausing in the B6J and B6J-*nmf205*$^{-/-}$ mice is specific to AGA codons, we compared codon frequency at (P ≥ 10) pause sites to the overall codon usage in transcripts. Although minor deviations were observed for several other codons,
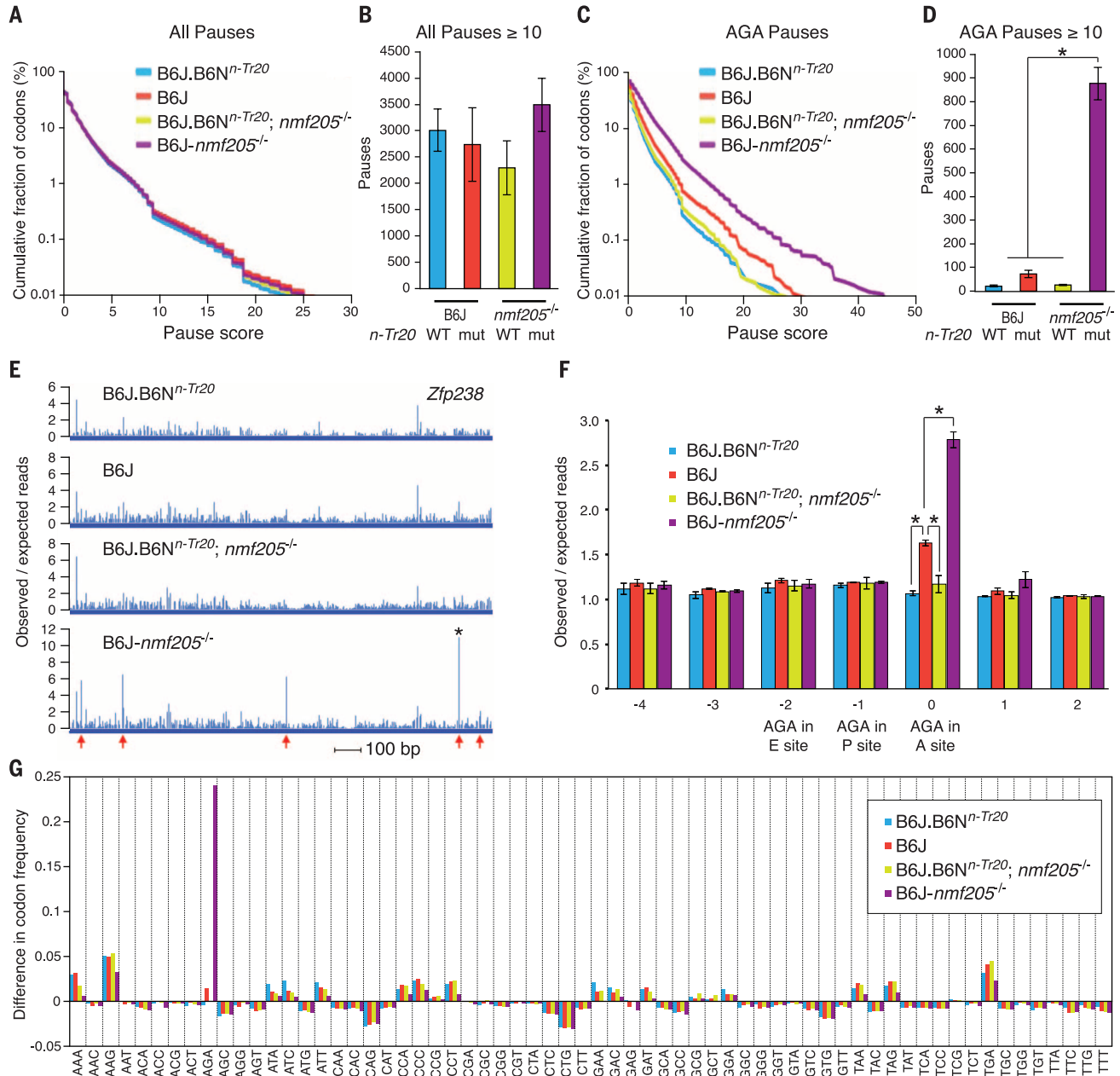
Fig. 4. The *n-Tr20* mutation induces ribosome stalling, which is resolved by GTPBP2. (**A**) Cumulative distribution of pauses at all codons averaged between replicates. (**B**) The mean number of pauses ≥10 standard deviations above the background translation levels of their genes (P ≥ 10). (**C**) Cumulative distribution of pause scores at AGA codons averaged between replicates. (**D**) The mean number of pauses (P ≥ 10) at AGA codons. (**E**) Read profile for *Zfp238* coding sequence. Asterisk (*) indicates an AGA pause with P = 45.

(See fig. S16.) Arrows indicate AGA codons. (**F**) Average pausing magnitude at AGA codons, calculated by dividing genome-wide observed reads at AGA codons by expected reads. Expectations are based on read densities in genes containing an AGA. Error bars indicate standard deviations across biological replicates. *P < 0.05 (two-tailed Student's *t* test). (**G**) Difference in the codon frequency observed in the A site at pauses (P ≥ 10) versus the genome-wide codon frequency.

the strain-specific AGA effect was much larger than any other effect, which demonstrated that the increase in ribosome pausing during translation in the B6J and B6J-*nmf205⁻/⁻* cerebellum occurs specifically at AGA codons (Fig. 4G).

Our data demonstrate that loss of function of a nuclear encoded tRNA induces ribosome stalling that is normally resolved by GTPBP2 (fig. S17). Note that Hbs1l, another ubiquitously expressed Pelota-binding partner, does not rescue neurodegeneration in the absence of GTPBP2, which is consistent with nonoverlapping functions of these proteins (fig. S4B) (*19*). In addition, the tissue-specific expression of *n-Tr20* suggests that the regulation of individual isodecoder tRNAs may enable translational regulation in mammals. Further, our finding of a pathogenic mutation in one isodecoder of a five-member gene family underlines the possible deleterious consequences of epistatic mutations in individual members of cytoplasmic tRNA genes that could affect the readout of other mutations, including synonymous SNPs. Finally, these data also emphasize the potential for regulation and disease of mutations in individual members of multicopy gene families.

REFERENCES AND NOTES

1. Genomic tRNA database; http://gtrnadb.ucsc.edu.
2. J. M. Goodenbour, T. Pan, *Nucleic Acids Res.* **34**, 6137–6146 (2006).
3. J. R. Buchan, I. Stansfield, *Biol. Cell* **99**, 475–487 (2007).
4. S. D. Moore, R. T. Sauer, *Mol. Microbiol.* **58**, 456–466 (2005).
5. K. Rooijers, F. Loayza-Puch, L. G. Nijtmans, R. Agami, *Nat. Commun.* **4**, 2886 (2013).
6. D. Goldowitz *et al.*, *Brain Res. Mol. Brain Res.* **132**, 105–115 (2004).
7. T. E. Dever, R. Green, *Cold Spring Harb. Perspect. Biol.* **4**, a013706 (2012).
8. V. P. Pisareva, M. A. Skabkin, C. U. Hellen, T. V. Pestova, A. V. Pisarev, *EMBO J.* **30**, 1804–1817 (2011).
9. C. J. Shoemaker, D. E. Eyler, R. Green, *Science* **330**, 369–372 (2010).
10. L. Levinger, D. Serjanov, *RNA Biol.* **9**, 283–291 (2012).
11. L. Levinger *et al.*, *J. Biol. Chem.* **270**, 18903–18909 (1995).
12. H. Kudo, S. Senju, H. Mitsuya, Y. Nishimura, *Biochem. Biophys. Res. Commun.* **272**, 456–465 (2000).
13. M. Watanabe *et al.*, *Gene* **256**, 51–58 (2000).
14. N. T. Ingolia, G. A. Brar, S. Rouskin, A. M. McGeachy, J. S. Weissman, *Nat. Protoc.* **7**, 1534–1550 (2012).
15. N. T. Ingolia, S. Ghaemmaghami, J. R. Newman, J. S. Weissman, *Science* **324**, 218–223 (2009).
16. N. T. Ingolia, L. F. Lareau, J. S. Weissman, *Cell* **147**, 789–802 (2011).
17. K. Yanagitani, Y. Kimata, H. Kadokura, K. Kohno, *Science* **331**, 586–589 (2011).
18. Materials and methods are available as supplementary material on *Science* Online.
19. N. R. Guydosh, R. Green, *Cell* **156**, 950–962 (2014).

CLATHRIN ADAPTORS

AP2 controls clathrin polymerization with a membrane-activated switch

Bernard T. Kelly,[1]* Stephen C. Graham,[2] Nicole Liska,[1] Philip N. Dannhauser,[3] Stefan Höning,[4] Ernst J. Ungewickell,[3] David J. Owen[1]*

Clathrin-mediated endocytosis (CME) is vital for the internalization of most cell-surface proteins. In CME, plasma membrane–binding clathrin adaptors recruit and polymerize clathrin to form clathrin-coated pits into which cargo is sorted. Assembly polypeptide 2 (AP2) is the most abundant adaptor and is pivotal to CME. Here, we determined a structure of AP2 that includes the clathrin-binding β2 hinge and developed an AP2-dependent budding assay. Our findings suggest that an autoinhibitory mechanism prevents clathrin recruitment by cytosolic AP2. A large-scale conformational change driven by the plasma membrane phosphoinositide phosphatidylinositol 4,5-bisphosphate and cargo relieves this autoinhibition, triggering clathrin recruitment and hence clathrin-coated bud formation. This molecular switching mechanism can couple AP2's membrane recruitment to its key functions of cargo and clathrin binding.

Clathrin adaptors provide an essential physical bridge connecting clathrin, which itself lacks membrane binding activity (*1*), to the membrane and to embedded transmembrane protein cargo. A central player in clathrin-mediated endocytosis (CME) is the AP2 (assembly polypeptide 2) complex (Fig. 1A and fig. S1), which both coordinates clathrin-coated pit (CCP) formation and binds the many cargo proteins that contain acidic dileucine and YxxΦ endocytic motifs (Y denotes Tyr; x, any amino acid; and Φ, a bulky hydrophobic residue) through its membrane-proximal core (*2, 3*). Cargo binding is activated by a large-scale conformational change from the "locked" or inactive cytosolic form to an "open" or active form driven by localization to membranes containing the plasma membrane phosphoinositide phosphatidylinositol 4,5-bisphosphate [PtdIns(4,5)P$_2$] (*4, 5*). The C-terminal "appendages" of the α and β2 subunits bind other clathrin adaptors as well as CCV (clathrin-coated vesicle) assembly and disassembly accessory factors (*3, 6–8*). The flexible hinge separating the β2 appendage from the β2 trunk binds the N-terminal β-propeller of the clathrin heavy chain by using a canonical clathrin box motif [LLNLD; L, Leu; N, Asn; D, Asp (Fig. 1, A and B)] (*9*). The β2 appendage domain also binds clathrin, albeit weakly, but both interactions are necessary for robust clathrin binding (*10*).

A version of AP2 comprising full-length β2, μ2, and σ2 subunits and the α trunk domain (FLβ.AP2) (Fig. 1B) (*11*) was expressed in *Escherichia coli*, avoiding contamination with other CCV components inherent to purification from brain tis-

[1]Cambridge Institute for Medical Research (CIMR), Department of Clinical Biochemistry, University of Cambridge, Hills Road, Cambridge CB2 0XY, UK. [2]Department of Pathology, University of Cambridge, Tennis Court Road, Cambridge CB2 1QP, UK. [3]Department of Cell Biology, Center of Anatomy, Hannover Medical School, Carl-Neuberg Strasse 1, D-30625 Hannover, Germany. [4]Institute of Biochemistry I and Center for Molecular Medicine Cologne, University of Cologne, Joseph-Stelzmann-Strasse 52, 50931 Cologne, Germany.
*Corresponding author. E-mail: btk1000@cam.ac.uk (B.T.K.); djo30@cam.ac.uk (D.J.O.).

sue (*12, 13*). Despite most FLβ.AP2 possessing an intact β2 subunit (Fig. 1, C to E), it bound clathrin very poorly in pulldowns when immobilized either on glutathione sepharose beads (Fig. 1C) or via its N-terminal His$_6$ tag [similarly positioned to the β2 PtdIns(4,5)P$_2$ binding site (Fig. 1B) (*4, 5*)] to liposomes containing the nickel-attached nitrilotriacetic acid–dioleoylglycerosuccinyl (NiNTA-DGS) (Fig. 1E): In both cases, the FLβ.AP2 will be in its locked cytosolic conformation (*4*). FLβ.AP2 also failed to stimulate clathrin cage assembly efficiently at physiological pH (Fig. 1D). In contrast, the isolated β2 hinge-appendage [glutathione S-transferase (GST)-β2-h+app (fig. S1)] bound clathrin efficiently (Fig. 1C) and stimulated cage assembly (Fig. 1D). We next compared clathrin recruitment to synthetic liposomes composed of dioleoylphosphatidylcholine and dioleoylphosphatidylethanolamine supplemented either with NiNTA-DGS or with a mixture of PtdIns(4,5)P$_2$ and a lipid-linked YxxΦ endocytic motif (*5, 11, 14*). β2-h+app fused to His$_6$-tagged epsin N-terminal homology (ENTH) domain (His$_6$-ENTH-β2-h+app), which can bind NiNTA-DGS or PtdIns(4,5)P$_2$, recruited clathrin efficiently to both types of liposomes. In contrast, FLβ.AP2 recruited clathrin only when bound to PtdIns(4,5)P$_2$- and YxxΦ-containing liposomes (Fig. 1E). Thus, no additional proteins are required to prevent clathrin binding to AP2 in solution, consistent with immunoprecipitation data (*15*). We conclude that the clathrin-binding activity of AP2 is autoinhibited in the cytosol to restrict inappropriate clathrin recruitment and that only upon encountering its physiological membrane ligands [PtdIns(4,5)P$_2$ and cargo] can AP2 recruit clathrin efficiently. Previous reports that AP2 purified from brain could bind and polymerize clathrin (*12*) were likely due to other contaminating clathrin adaptors, such as AP180 (*13*).

We were unable to crystallize FLβ.AP2, so we determined the structure of a form of AP2 (βhingeHis$_6$.AP2) whose β2 (residues 1 to 650) includes the clathrin box–containing hinge but not the β2 appendage. The structure closely

Science
AAAS

Ribosome stalling induced by mutation of a CNS-specific tRNA causes neurodegeneration
Ryuta Ishimura *et al.*
Science **345**, 455 (2014);
DOI: 10.1126/science.1249749

This copy is for your personal, non-commercial use only.